J. Fluid Mech. (1985), *vol.* 158, *pp.* 1–22
Printed in Great Britain

Shallow rotating flow over an isolated obstacle

By V. R. LAMB AND G. S. JANOWITZ

Department of Marine, Earth, and Atmospheric Sciences, North Carolina State University, Raleigh, NC 27695–8208

(Received 20 September 1982 and in revised form 22 February 1985)

The deflection of flow around an isolated obstacle in a rotating homogeneous fluid is investigated. Criteria for the onset of closed streamlines over an isolated obstacle are reviewed. In the flow regime where no closed streamlines exist, steady solutions for the stream function are obtained for both quasigeostrophic and finite-Rossby-number flows. A measure is proposed to allow quantitative evaluation of the flow patterns, and the dependence of deflection on obstacle volume and aspect ratio is examined. In the regime where closed streamlines can exist, the presence of a trapped vortex to the right (looking downstream) of the obstacle is investigated by means of time integration of the shallow-water equations. The significance of the trapped vortex for a real fluid is then tested through the addition of the frictional effect of Eckman pumping.

1. Introduction

1.1. *Statement of the problem*

The problem of predicting fluid flow in complex terrain is one of great current interest to meteorologists as well as oceanographers. At this point, however, our understanding even of the flow of a rotating homogeneous fluid over and around a single obstacle of simple shape is still incomplete.

For flows with no closed streamlines, i.e. for which all streamlines can be considered to originate upstream, a basic question concerns the dependence of flow over versus flow around the topography on the parameters of the problem. The physical quantities needed to specify flow over a hill of heightscale h_m and length- and widthscales l_x and l_y respectively in a shallow fluid with a free surface of mean depth h_0 and of infinite horizontal extent, with Coriolis parameter f, can be combined into five dimensionless parameters: relative hill height $h^* \equiv h_m/h_0$, aspect ratio $A \equiv l_y/l_x$, h_m/l_x, Rossby number $Ro \equiv u_0/fl_x$ and rotational Froude number $Fr \equiv f^2l_x^2/gh_0$.

Most recently, Bannon (1980) investigated the dependence of flow deflection on many factors, including dissipation, rotation (Ro) and free-surface effect (Fr). Many of his results may be affected by the particular representation of friction included in the model, but for an aspect ratio $A = 1$ the dependence on Ro and Fr is reasonably clear and verifies the results of previous studies (e.g. Vaziri & Boyer 1971). He also showed that an obstacle with its long axis aligned normal to the inflow causes greater blocking and a more asymmetric response than the same obstacle with its long axis downstream. His measure of deflection, however, gives little information about the resultant streamline patterns as an aid in predicting the flow for other values of A or Ro. A more systematic examination of dependence on obstacle shape remains to be done, and is the first goal of the present work.

A criterion defining, for a circularly symmetric obstacle, the values of Ro and h^*

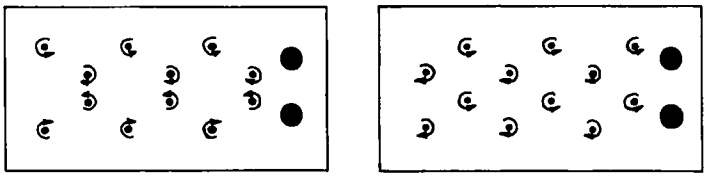

(*a*) Antiphase (*b*) In phase

FIGURE 1. Idealized vortex configurations in the wake of a pair of bluff bodies normal to a stream. (*a*) Two parallel streets in antiphase from antiphase vortex shedding. (*b*) Two parallel streets in phase from in-phase vortex shedding. Cylinders translating from left to right.

are markedly higher than for the other cylinder (for example see Spivack 1946). The gap flow becomes stably deflected to the high-frequency side of the wake, and the cylinder on this side experiences a greater drag force than the other cylinder. There exists a mean repulsive lift force between the cylinders. The structure of the near wake has been previously shown from flow visualization to be confused in this 'asymmetric-flow regime', and very little has been deduced about the form of the wake flow. However, the deflection of the gap flow has been demonstrated (Ishigai *et al.*, Bearman & Wadcock, Quadflieg) for Reynolds number in the region of 10^4 or above.

The total cylinder-pair drag force increases as gaps are reduced from $g^* = 4.0$ to 1.0. For smaller gaps the combined drag can become less than twice the isolated-cylinder drag (for example, Bierrman & Herrnstein 1933; Quadflieg).

The present paper mainly involves flow visualization behind a pair of circular cylinders, and also behind a pair of flat plates normal to a steady stream. Dye- and smoke-visualization techniques are used. Where antiphase-vortex-shedding synchronization occurs the visualization in §3 clearly demonstrates that the resulting wake is a pair of antiphase parallel streets as found in other studies. However, in-phase shedding at the cylinders does not lead to two in-phase parallel streets as previously supposed, but rather to a large-scale combined wake. The like-signed vortices pair up and a 'binary-vortex' street is formed. Flow visualization in §4 also shows that, when the bodies are sufficiently close to produce an asymmetric wake, there is a distinct mode of shedding when the vortex-shedding frequency on one side of the wake is a multiple of that on the other side. Such a harmonic mode of vortex shedding has hitherto not been suggested.

2. Experimental methods

The present study of the vortex wakes of two bodies involves flow visualization using both smoke in a wind tunnel and dye in a water channel. For the smoke visualization a vertical low-speed wind tunnel with upward flow is used, which has a working section 12×6 in. in cross-section, and is 20 in. long. Two side-by-side cylinders of external diameter 0.043 in. spanning the shortest dimension of the working section were used to generate the vortex wakes. We assume blockage is negligible because the ratio of the channel width to cylinder diameter is 280:1. The 'smoke' is actually liquid kerosene in the form of fine droplets formed in a smoke generator of the Preston & Sweeting (1943) type. Reynolds numbers were in the range 50–150. A Nikon camera is used in both methods of visualization (with 1 ms exposure times when using smoke). The smoke is illuminated by two 1000 W halogen bulbs providing a slit of light halfway along the length of the cylinders.

For the dye visualization a closed-circuit water channel is used of depth 10 cm with

that each streamline originates upstream, then (1) implies that the potential vorticity is conserved along each streamline and

$$\frac{\zeta+f}{h_0-h_s}=\frac{\zeta_{-\infty}+f}{h_0}. \tag{2}$$

If a uniform flow is assumed upstream and far from the obstacle, $u_{-\infty}=u_0$, $v_{-\infty}=0$. Then $\zeta_{-\infty}=0$ and

$$\zeta=-\frac{fh_s}{h_0}. \tag{3}$$

This vorticity balance follows strictly from the assumptions of shallow water and no closed streamlines. If we now assume that the Rossby number based on obstacle width is infinitesimal, then $\boldsymbol{v}\approx\boldsymbol{v}_g=\boldsymbol{k}\times\nabla\psi_g$ and

$$\nabla^2\psi_g+\frac{fh_s}{h_0}=0, \tag{4}$$

with $\nabla\psi_g\sim(0,\,-u_0)$ far from the obstacle. From (4) it follows that the circulation about the obstacle is equal to $-f/h_0$ times the obstacle volume. The quasigeostrophic vorticity equation (4) could of course be derived without the shallow-water assumption used in (1) by assuming the flow to be inviscid, homogeneous, steady, of infinitesimal Rossby number, with uniform flow upstream and all streamlines originating upstream.

For axisymmetric obstacles, cylindrical coordinates are convenient, and ψ_g can be expressed in the form

$$\psi_g=-u_0 r\sin\theta+\tilde{\psi}(r), \tag{5}$$

so that (4) gives

$$\frac{1}{r}\frac{\mathrm{d}}{\mathrm{d}r}(r\tilde{\psi}_r)+\frac{fh_s}{h_0}=0, \tag{6}$$

and integrating once yields

$$\frac{\mathrm{d}\tilde{\psi}}{\mathrm{d}r}=-\frac{f}{h_0 r}\int_0^r th_s(t)\,\mathrm{d}t. \tag{7}$$

Note that the obstacle height appears only under an integral, so that at least away from the obstacle the net volume determines the velocity perturbation. Equation (7) can be integrated to determine ψ, and thus the streamlines, explicitly.

A criterion for the existence of a stagnant region, or inertial Taylor column, is found by determining when a stagnation point, i.e. a point where $\psi_\theta=\psi_r=0$, exists in the flow. It is straightforward to obtain from (5) and (7) (Huppert 1975) that stagnation points can exist only for $\theta=-\frac{1}{2}\pi$ and r such that

$$\frac{f}{h_0 u_0}=\frac{r}{\int_0^r th_s(t)\,\mathrm{d}t}. \tag{8}$$

For example, for the cone $h_s(r)=h_m(1-r/a)$, a value of r exists that satisfies (8) if

$$\delta\equiv\frac{h_m}{h_0 Ro}=\frac{h^*}{Ro}\geqslant\tfrac{16}{3}\equiv\delta_S, \tag{9}$$

where $Ro=u_0/fa$. For $\delta>\delta_S$ (4) no longer holds as closed streamlines will exist.

To investigate motions at finite Rossby number over topography of finite height, Johnson (1978) has examined steady solutions to the equations for hydrostatic

motions in an inviscid homogeneous fluid with a horizontal upper surface. Following his derivation, the non-divergence of the mass flux $h\boldsymbol{v}$, where $h \equiv h_0 - h_s(r)$, allows us to define a stream function such that

$$\boldsymbol{v}^* \equiv h\boldsymbol{v} = \boldsymbol{k} \times \nabla\psi^*. \tag{10}$$

Vorticity can then be expressed in terms of ψ^* as follows:

$$\zeta = \frac{\partial v}{\partial x} - \frac{\partial u}{\partial y} = \frac{\partial}{\partial x}\left(\frac{1}{h}\frac{\partial \psi^*}{\partial x}\right) + \frac{\partial}{\partial y}\left(\frac{1}{h}\frac{\partial \psi^*}{\partial y}\right) = \mathrm{L}(\psi^*), \tag{11}$$

and for a uniform upstream flow we have, as in (3),

$$\zeta = -\frac{fh_s}{h_0}. \tag{12}$$

For axisymmetric topography it is convenient to split ψ^* into ψ_1^* and ψ_2^*, where

$$\psi_1^* = \sin\theta\, F(r), \quad \psi_2^* = G(r), \tag{13a, b}$$

with

$$\mathrm{L}(\psi_1^*) = 0 \quad \text{and} \quad \mathrm{L}(\psi_2^*) = -\frac{fh_s}{h_0}. \tag{14a, b}$$

Far from the obstacle $\boldsymbol{k} \times \nabla\Psi_1^* \to u_0 \boldsymbol{i}$ and $\boldsymbol{k}^* \nabla\psi_2^* \to \boldsymbol{0}$. Equations (14) can be solved, and an expression for the total stream function ψ^* obtained:

$$\psi^* = -u_0 \sin\theta(r + R(r)) - \frac{f}{h_0}\int_0^r \frac{h(t)}{t}\int_0^t s h_s(s)\,\mathrm{d}s\,\mathrm{d}t, \tag{15}$$

where $R(r)$ satisfies

$$\frac{h}{r}\left(\frac{rR_r}{h}\right)_r - \frac{R}{r^2} = \frac{h_r}{h}. \tag{16}$$

For solution (15) a stagnation point first occurs at $\theta = -\frac{1}{2}\pi$ and r such that

$$u_0 = \frac{fh}{rh_0^2}\frac{1}{1+R_r}\int_0^r t h_s(\tau)\,\mathrm{d}\tau. \tag{17}$$

For a conical obstacle the critical values of $h^* = h_m/h_0$ are found numerically from (16) and (17) and plotted in figure 1 as the dashed curve. The quasigeostrophic result ($Ro = \frac{3}{16}h^*$) from (9) is given as the solid line. The comparison of the two curves in figure 1 demonstrates that the quasigeostrophic solution underestimates the obstacle height required to cause closed streamline solutions for a given Ro.

In §2 steady solutions for the quasi-geostrophic case (4) and the finite-Rossby-number case (11) and (12) are obtained numerically in a systematic investigation of dependence of flow deflection on obstacle shape. A measure of streamline deflection is proposed and curves of dependence are constructed allowing prediction of streamline patterns as a function of obstacle-shape parameters.

For the case $\delta > \delta_S$, in a flow starting up from rest, conservation of potential vorticity specifies that a region of negative relative vorticity is generated as fluid from upstream rises over the obstacle, creating a vortex bound to the topography. The column of fluid initially at rest over the obstacle, having a larger value of the potential vorticity than the surrounding fluid by virtue of shorter column height, will be stretched as it descends to the lee and a region of positive vorticity will be generated. It is plausible that for relatively strong oncoming flow the cyclonic eddy will move off downstream, while for relatively weak flow the interaction between the anticyclonic and cyclonic vortices will trap the eddy, as shown by Huppert & Bryan (1976).

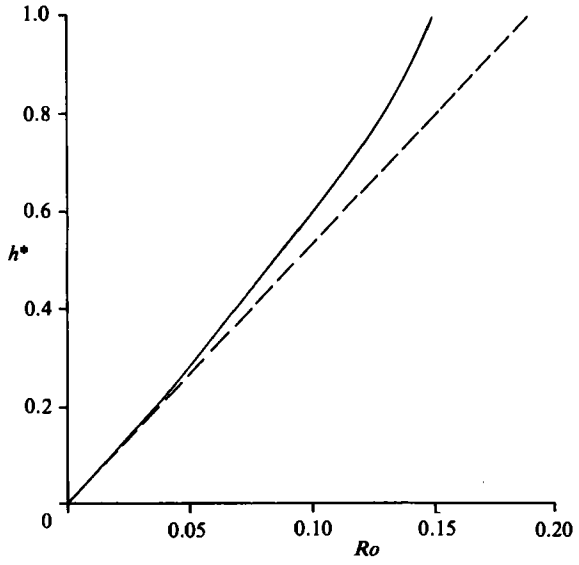

FIGURE 1. Critical h^* versus Ro for the existence of stagnation points in the flow around a cone: quasigeostrophic solution (9) (dashed); finite-Ro solution (17) (solid).

In §3 a time-dependent finite-difference model is formulated, and the results of integrations testing the criterion for formation of closed streamlines and existence of a trapped eddy are presented. In §4 are presented the conclusions of the study.

2. Deflection of flow in the regime with no closed streamlines

2.1. *Parameter dependence of deflection*

Some insight into the general parameter dependence of streamline deflection can be achieved through the following argument. For a homogeneous fluid with a horizontal upper surface of height h_0, consider the class of geometrically similar obstacles on the lower surface whose height can be expressed in the form

$$h_s = h_m \bar{h}\left(\frac{x}{l_x}, \frac{y}{l_x}\right). \tag{18}$$

Here, instead of defining a stream function based on the mass flux as in (10), we write the velocity components in terms of irrotational (ϕ) and non-divergent (ψ) parts, so that

$$u = u_0 - \psi_y + \phi_x, \quad v = \psi_x + \phi_y, \tag{19}$$

where the vorticity equation, for uniform upstream flow, is again given by

$$\zeta = \nabla^2\psi = \frac{-fh_s}{h_0}. \tag{20}$$

We define $(\bar{x}, \bar{y}) = (x, y)/l_x$, $\bar{\psi} = \psi/\psi_r$, and $A = l_y/l_x$ is the aspect ratio. Then (20) becomes

$$\frac{\psi_r}{l_x^2}\bar{\nabla}^2\bar{\psi} = -\frac{fh_m}{h_0}\bar{h}\left(\bar{x}, \frac{\bar{y}}{A}\right).$$

We now take $\psi_r \equiv (fh_m/h_0)\, l_x l_y$, and so

$$\bar{\nabla}^2\bar{\psi} = -\frac{\bar{h}(\bar{x}, \bar{y}/A)}{A}. \tag{21}$$

Since $\int_0^1\int_0^A \bar{h}\,\mathrm{d}\bar{x}\,\mathrm{d}\bar{y} = O(A)$, $\bar{\psi} = O(1)$. Thus $\bar{\psi} = \bar{\psi}(\bar{x}, \bar{y}, A)$ for a given $\bar{h}$. Now the continuity equation for the fluid is the condition of non-divergence of mass flux:

$$\frac{\partial}{\partial x}[u(h_0 - h_s)] + \frac{\partial}{\partial y}[v(h_0 - h_s)] = 0.$$

Using (19), this becomes

$$(h_0 - h_s)\,\nabla_H^2\phi - \nabla\phi\cdot\nabla h_s = \psi_x h_{sy} - \psi_y h_{sx} + u_0 h_{sx}. \tag{22}$$

We let $$\phi = \phi_r\bar{\phi},$$

and $$\phi_r = \psi_r = \frac{fh_m l_x l_y}{h_0}.$$

Then (22) becomes, defining $h^* \equiv h_m/h_0$,

$$(1 - h^*\bar{h})\,\bar{\nabla}^2\bar{\phi} - h^*\bar{\nabla}\bar{\phi}\cdot\bar{\nabla}\bar{h} = h^*[\bar{\psi}_{\bar{x}}\bar{h}_{\bar{y}} - \bar{\psi}_{\bar{y}}\bar{h}_{\bar{x}}] + \frac{Ro}{A}\bar{h}_{\bar{x}}. \tag{23}$$

Thus, for a given $\bar{h}(\bar{x}, \bar{y}, A)$, (21) gives that $\bar{\psi} = \bar{\psi}(\bar{x}, \bar{y}, A)$, and, from (23), $\bar{\phi} = \bar{\phi}(A, h^*, R_0)$.

An expression for the streamline deflection can be written, using (19),

$$\frac{\mathrm{d}\bar{y}}{\mathrm{d}\bar{x}} = \frac{v}{u} = \frac{\bar{\psi}_{\bar{x}} + \bar{\phi}_{\bar{y}}}{\dfrac{u_0 l_x}{\psi_r} - \bar{\psi}_{\bar{y}} + \bar{\phi}_{\bar{x}}}.$$

Since $$\frac{u_0 l_x}{\psi_r} = \frac{R_0 l_x^2 h_0}{l_x l_y h_m},$$

if we define a volume parameter

$$\bar{V} \equiv \frac{h_m l_x l_y}{R_0 h_0 l_x^2} = \frac{h^* A}{Ro},$$

then $$\frac{\mathrm{d}\bar{y}}{\mathrm{d}\bar{x}} = F(\bar{V}, A, Ro, \bar{x}, \bar{y}). \tag{24}$$

For the quasigeostrophic case, i.e. as $Ro \to 0$ with $\bar{V}$ and A fixed ($h^* \to 0$), then $\bar{\phi} \to 0$ and

$$\frac{\mathrm{d}\bar{y}}{\mathrm{d}\bar{x}} = F(\bar{V}, A, \bar{x}, \bar{y}). \tag{25}$$

Thus for quasigeostrophic flows the deflection must depend only on $\bar{V}$ for fixed A, i.e. on h^*/Ro. Since a cone satisfies the class of obstacles (18), it is clear that all points on the critical curve $h^*/Ro = \frac{16}{3}$ (solid line) in figure 1 correspond to the same deflection pattern, which would be the maximum deflection possible in the regime with no closed streamlines.

The data in figure 1 are replotted in figure 2 in terms of the new volume parameter $\bar{V}$ and Ro ($A = 1$). The ordinate intercept is the quasigeostrophic value $\bar{V} = h^*/Ro = \frac{16}{3}$, the limiting value as $Ro \to 0$. The other points are taken from the

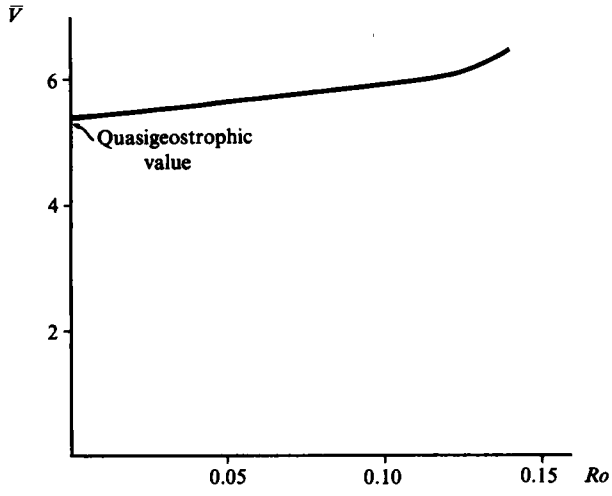

FIGURE 2. Critical $\bar{V}$ versus *Ro* for the existence of stagnation points in flow around a cone.

finite-*Ro* solution (17), the dashed line of figure 1. The usefulness of the new parameter is evident; the plot shows clearly the effect of finite *Ro*.

2.2. *The experimental obstacle*

We wish to examine numerically the effect of aspect ratio on the flow field. As the critical curve for flow around a cone has been established, this shape was chosen as the case $A = 1$. To widen the obstacle in the cross-stream direction, a ridge of triangular cross-section was inserted between the two halves of the cone, as depicted in figure 3(*a*). The aspect ratio was defined as $A = l_y/l_x$. The volume of such an obstacle, normalized by $Ro\, h_0\, l_x^2$, can be expressed as

$$V^* \equiv \frac{h^*}{Ro}[\tfrac{1}{3}\pi + 2(A-1)] = \bar{V}\left(2 - \frac{0.95}{A}\right).$$

The chosen obstacle is not expressible in the form (18). However, the deflections can be shown to depend only on $\bar{V}$ and A or, equivalently, V^* and A. In describing our results, V^* and A will be used.

2.3. *The measure of deflection*

In order to compare deflection of the flow for various cases it was necessary to devise a quantitative measure of the flow around an obstacle. To this end, consider the streamline that just passes over the centre of the obstacle, as shown in the schematic diagram of figure 3(*b*). The deviation of that streamline from the centreline of the channel at an arbitrary distance upstream gives an indication of the magnitude of the deflection of streamlines. A non-dimensional measure can then be defined through normalization by the downstream half-width of the obstacle l_x. In the following experiments the deflection was measured one cone diameter upstream from the obstacle centre, i.e. at $\bar{x} = -2$.

2.4. *The domain of solution*

The domain considered was a channel with rigid sidewalls at which $\partial\psi/\partial x = 0$. At the inflow boundary a constant zonal flow was specified, and at the outflow boundary

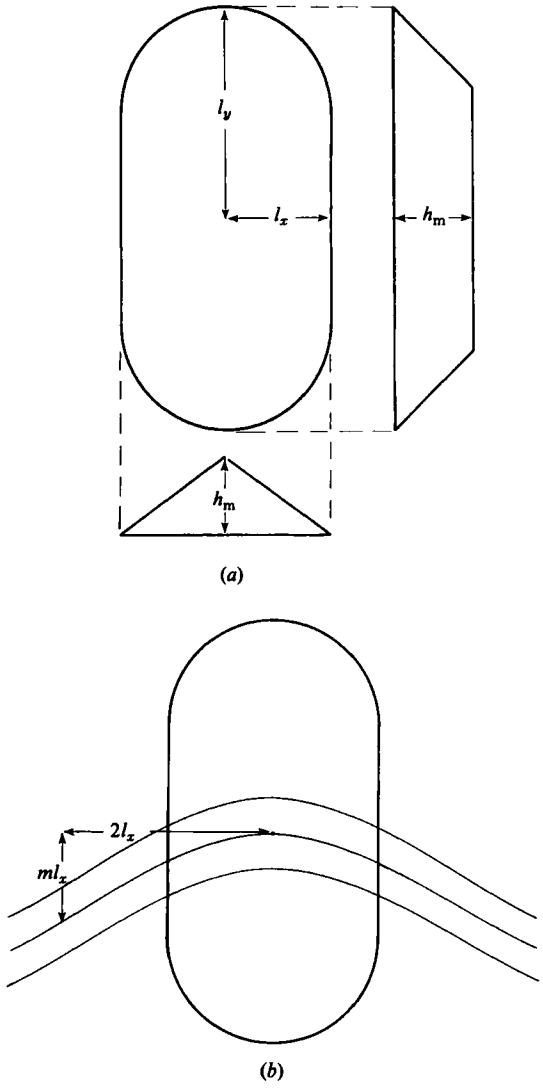

FIGURE 3. Schematic of obstacle showing lengths used to define (*a*) aspect ratio A, volume V^*; (*b*) the measure of deflection m.

a cyclic condition was applied. The intent was to achieve results arbitrarily close to those for an isolated obstacle on an infinite plane by considering a finite domain of sufficiently large dimensions.

It can be shown that a channel width cannot be uniquely determined such that the influence of the sidewalls on the flow pattern is within some bound. For quasigeostrophic flow the channel ($z = x + \mathrm{i}y$) can be mapped into a semi-infinite plane for the transformation

$$\zeta = \mathrm{i} \exp\left(\frac{\pi z}{2a}\right),$$

where a is the channel half-width, i.e. $y = \pm a$ are the channel walls, which map into

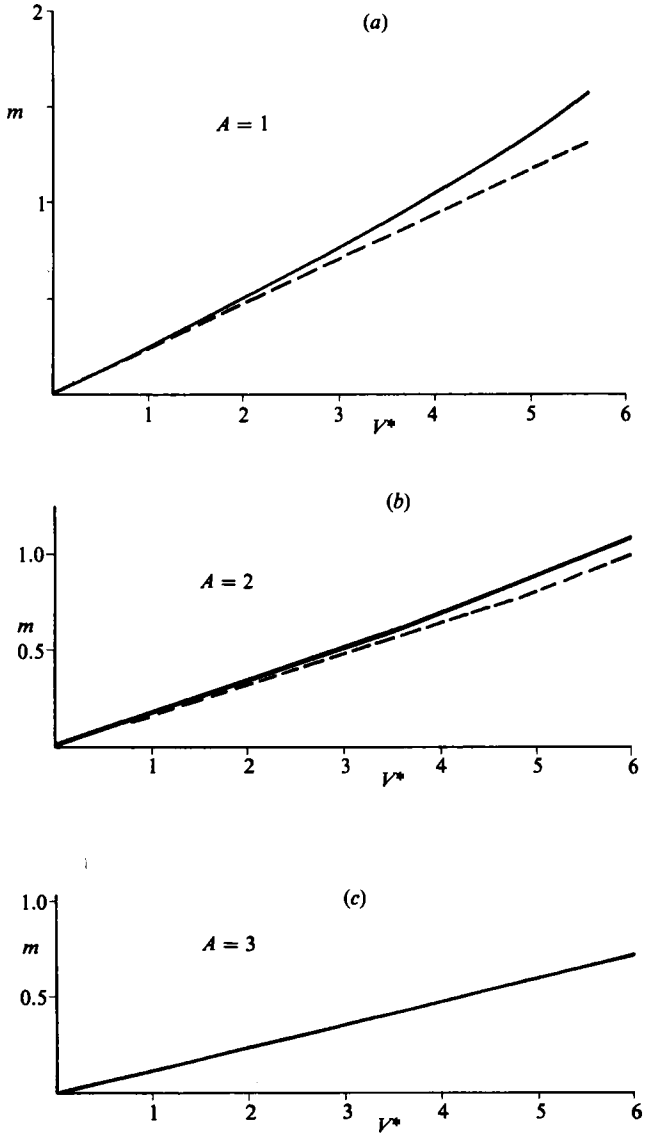

FIGURE 4. Results of experiments showing m as a function of V^* with A fixed: quasigeostrophic case (solid): finite-Ro case $Ro = 0.15$ (dashed).

the real ζ-axis. A point vortex of strength $-\Gamma$ at $z_0 = x_0 + iy_0$ maps to the point in the ζ-plane:

$$\zeta_0 = i \exp\left(\frac{\pi z_0}{2a}\right).$$

To ensure that there is no flow through the channel walls, a vortex of strength $+\Gamma$ must be placed at ζ_0^* in the ζ-plane. The stream-function perturbation at ζ due to the point vortex is then

$$\delta\Psi_g = \frac{-\Gamma}{2\pi} \ln\left|\frac{\zeta-\zeta_0}{\zeta-\zeta_0^*}\right|,$$

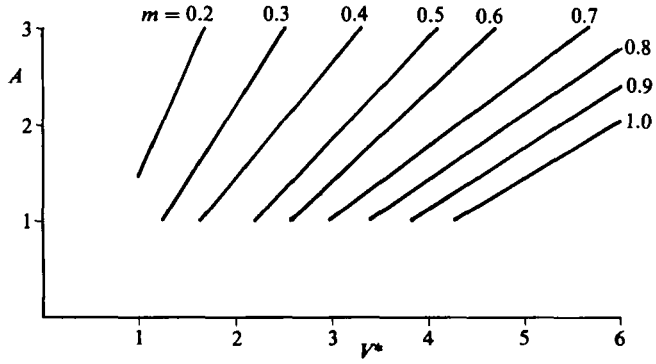

FIGURE 5. Contours of deflection measure m as a function of A and V^* for the finite-Ro case ($Ro = 0.15$).

where we can take Γ to be f/h_0 times the volume of an infinitesimal element of an extended topography.

For $|z|/a$ and $|z_0|/a \ll 1$ the disturbance due to an isolated portion of the extended topography can be expanded in a power series a^{-1}, and we obtain

$$\delta\Psi_g = \frac{-\Gamma}{2\pi}\left(\ln|x-x_0| + \frac{f_1(x_0, y_0)}{a} + \frac{f_2(x, y, x_0, y_0)}{a^2} + \ldots\right),$$

where f_1 is linear in x_0 and y_0, and f_2 is quadratic in terms of its arguments. The net effect on ψ_g due to an extended topography is the sum over all elements of volume of the topography. It is clear that the effect of the sidewalls varies both with the shape of the topography and with the location, and it is impossible to keep sidewall effects fixed while varying the topography. Thus the effect of channel dimension and grid resolution on the particular measure chosen was determined by numerical experiment, and the boundaries chosen far enough from the obstacle to have little effect on the measure of deflection and to simulate an unbounded domain (see the Appendix).

2.5. *The experiments*

For quasigeostrophic and finite-Ro flows, (4) and (12) respectively were solved by a standard iterative technique (SLOR). Experiments were performed for $A = 1.0$, 2.0, 3.0; for fixed A the variation with V is shown in figures 4(a–c). The solid curves are derived from solutions of the quasigeostrophic model and represent the limit as $Ro \to 0$. The dashed lines are drawn through values from the finite-Ro model, for $Ro = 0.15$. The effect of finite Ro is not large; in figure 4(c) the two curves are indistinguishable. For both models, the increase in deflection with volume for given aspect ratio is clearly seen.

Finite-Ro results are replotted to allow contours of m to be drawn as functions of A and V^*, shown in figure 5. These contours facilitate prediction of deflection for an obstacle of roughly similar shape and more general dimensions. As A increases with V^* fixed, deflection decreases, and, as V^* increases with A fixed, deflection increases.

3. Regime with closed streamlines

The numerical results presented here are derived from integration of initial-value problems based on the inviscid shallow-water equations. Including both the Coriolis term and the pressure-gradient term that arises in the presence of bottom topography

of height $h_s(x, y)$, the equations governing the perturbations to a resting state can be written

$$\frac{\partial}{\partial t}\boldsymbol{v}_H + \boldsymbol{v}_H \cdot \nabla_H \boldsymbol{v}_H + f\boldsymbol{k} \times \boldsymbol{v}_H = -\nabla_H g(h + h_s), \tag{26a}$$

$$\frac{\partial h}{\partial t} + \nabla_H \cdot h\boldsymbol{v}_H = 0, \tag{26b}$$

where h is the depth of the fluid column, and the Coriolis parameter $f = 10^{-4}\ \mathrm{s}^{-1}$ throughout.

If the initial free-surface perturbation η_0 is tilted such that the pressure is in geostrophic balance with a constant zonal flow u_0 for a channel with flat bottom, that is

$$\eta_0(y) = -\frac{f u_0 y}{g}, \tag{27}$$

then the initial state constitutes a steady solution in the absence of bottom topography. With bottom topography present (27) will not be exact in the vicinity of the obstacle, but does tend to minimize the amplitude of spurious components and deformation of the zonal flow field.

The arrangement of variables on the grid and the finite-difference scheme for (26) is that presented in Arakawa & Lamb (1983). The space-differencing scheme is of second-order accuracy and maintains finite-difference analogues of the laws of conservation of energy and mean-square potential vorticity that hold for such a fluid. Leapfrog differencing in time, a second-order scheme which is neutral for the linear case, was used. The weak instability that arises with the use of a three-level scheme in nonlinear equations was suppressed by a forward step inserted periodically. Although there are higher-order schemes that give better simulation of pure advection, in the present problem conservation of potential vorticity is of great importance and the chosen scheme has been shown (Arakawa & Lamb 1983) to give a good representation of topographically induced eddies.

The channel extended in x from $-L_x$ to $+L_x$, where, as in the steady solutions of §2, cyclic boundary conditions were assumed. A conical obstacle with a radius of 5 km was centred in a channel of 26 km width, 50 km length and 0.5 km depth, with a grid spacing of 1 km. The results of the Appendix for the steady problem with a rigid lid indicate that these dimensions give an adequate representation of flow on an unbounded plane, at least near the centre of the channel.

The effect of the free surface is to decrease slightly the vorticity and resultant acceleration generated by the column shortening as flow passes over the obstacle. In these experiments $Ro\,Fr = O(10^{-3})$, and the equilibrium horizontal surface in the asymptotic state can be shown sufficiently undisturbed that a good comparison to the rigid-lid solution is possible. A sample integration allows us to compare the model results with the finite-Ro rigid-lid solution (15). For values $Ro = 0.1$, $h^* = 0.5$, h^*/Ro is less than critical for a cone, and no closed streamlines should exist in the steady state. Figure 6 (*a*) shows velocity vectors from the time-dependent model after 6 days; velocity vectors derived from the analytical solution (15) and (16) for the same Rossby number are shown in figure 6 (*b*) for comparison. The solutions differ slightly at the sidewalls, but the solutions near the obstacle are very close.

The first point to be investigated is the significance of the criterion (17) for formation of a stagnation point in finite-Ro flow over a conical obstacle. For $h^* = 0.5$ the case $Ro = 0.1$ ($u_0 = 5$ cm/s), lying below the dashed curve in figure 1, should correspond to a flow with no closed streamlines. Velocity vectors for the case $Ro = 0.1$

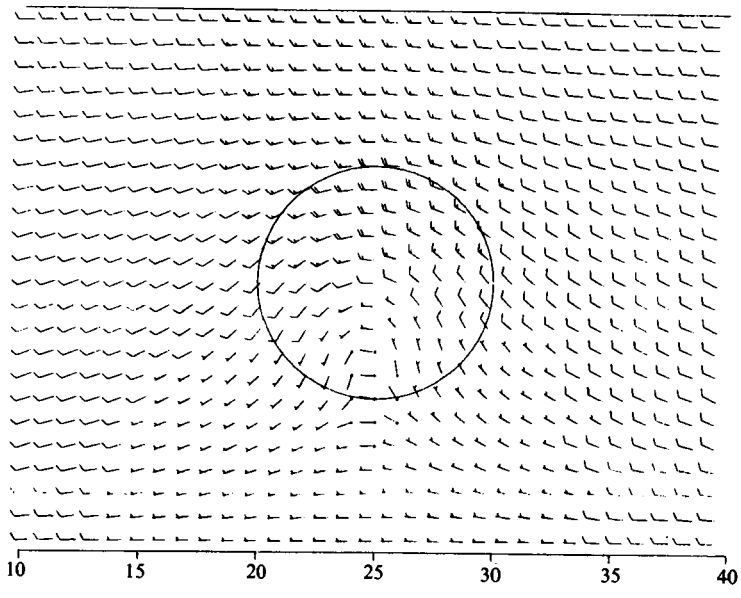

(a)

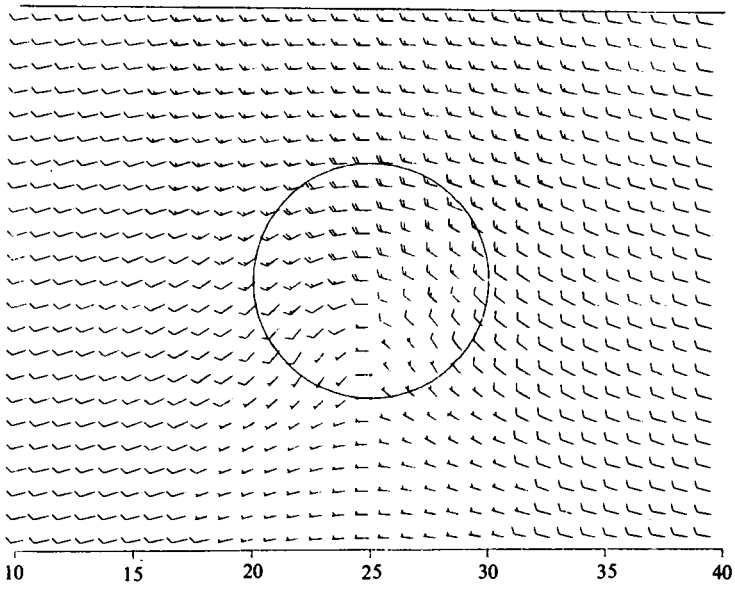

(b)

FIGURE 6. Results from the time integration for flow around a cone with $h^* = 0.5$, $Ro = 0.1$: (a) velocity vectors from solution of numerical model after 8 days integration; (b) velocity vectors from solution of (15).

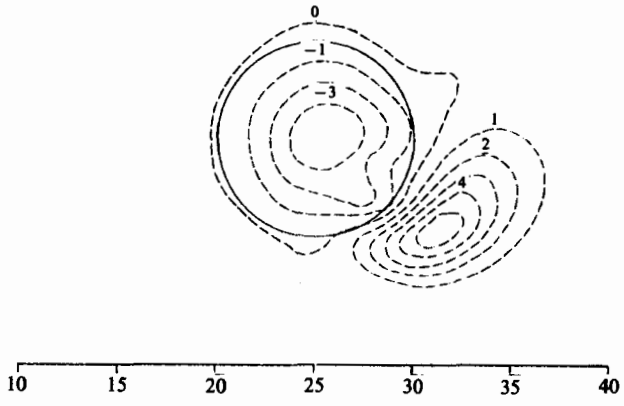

(*a*)

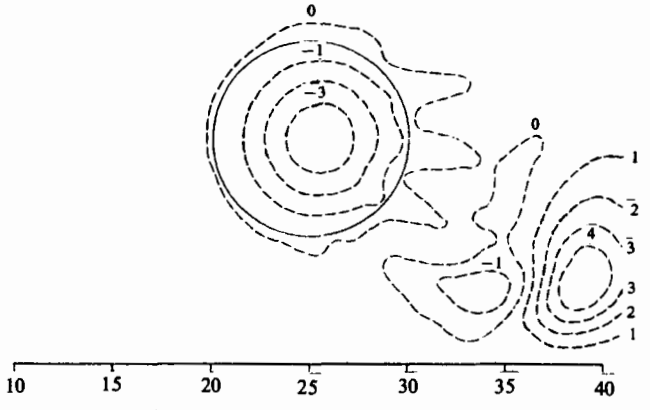

(*b*)

FIGURE 7. Results from the time integration for flow around a cone with $h^* = 5$, $Ro = 0.1$: contours of $10\zeta/f$ after (*a*) 2 days; (*b*) 4 days.

are shown in figure 6(*a*): after 6 days only the bound vortex is present and the flow is approaching the up- and downstream symmetry of the steady state. The plots of non-dimensional vorticity ($10\zeta/f$ is shown) for 2 and 4 days, shown in figures 7(*a*) and (*b*) respectively, clearly show the shed eddy being swept downstream. (The weak negative vortex trailing the shed eddy is an artifact of the space-differencing of the potential vorticity, created as the column of fluid initially over the obstacle is advected off the obstacle.)

The case $Ro = 0.075$ ($u_0 = 3.75$ cm/s) was chosen to investigate the transition between the trapped- and the shed-eddy regimes, where $\delta_S < \delta < \delta_T$ and for which Johnson's variational approach can give no information. This case is slightly above the dashed line and should correspond to a regime with closed eddy bound to the obstacle. Another eddy formed of fluid initially above the obstacle should form in the lee; whether this shed eddy is trapped near the obstacle in the steady state or is swept downstream is another point to be investigated. The non-dimensional vorticity $10\zeta/f$ is shown in figures 9(*a–c*) after 2, 4 and 6 days integration. The positive

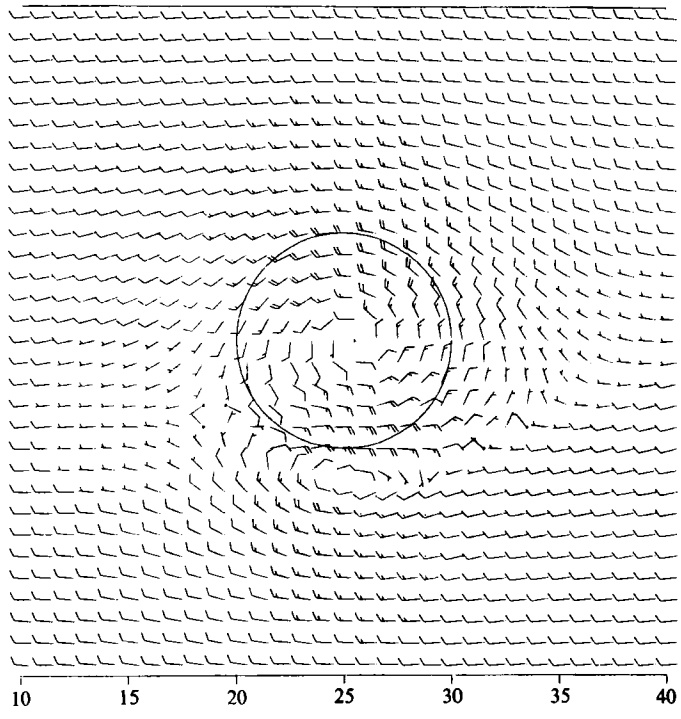

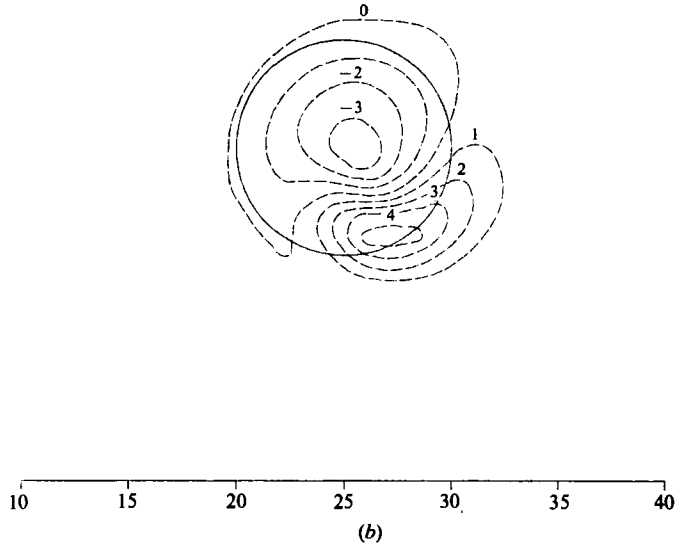

FIGURE 8(*a*,*b*). For caption see facing page.

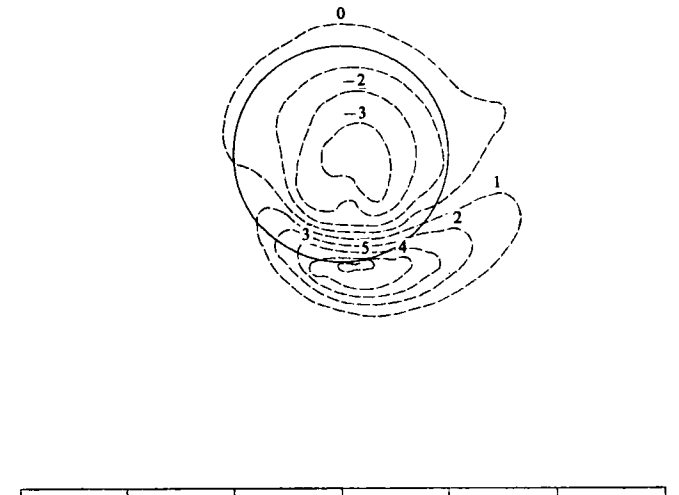

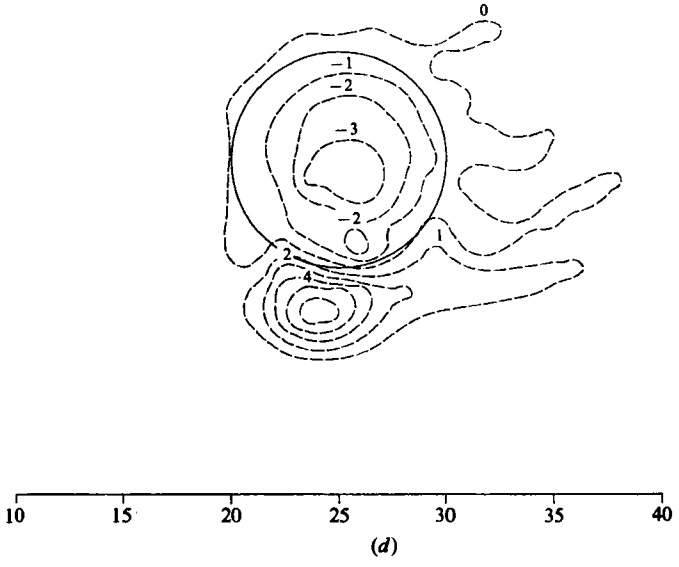

FIGURE 8. Results from the time integration for flow around a cone with $h^* = 0.5$, $Ro = 0.05$: (*a*) velocity vectors after 8 days; (*b*), (*c*), (*d*) contours of $10\zeta/f$ after respectively 2, 4, 10 days.

vortex is clearly shed downstream. If a transitional regime of partial trapping exists it is not evident at this Rossby number.

For $h^* = 0.5$ the case $Ro = 0.05$ ($u_0 = 2.5$ cm/s) is well above the dashed curve, and could be expected from the results of Johnson (1978) to correspond to trapping of the shed eddy by the bound eddy. The velocity vector pattern after 8 days for the case $Ro = 0.05$ is shown in figure 8(*a*), and the hypothesis of Johnson is verified, for there is a pair of eddies in the vicinity of the obstacle. The vortex on the right-hand side, looking downstream, is the shed eddy that has been trapped by the bound vortex over the obstacle. These vortices can be clearly identified by an examination of the

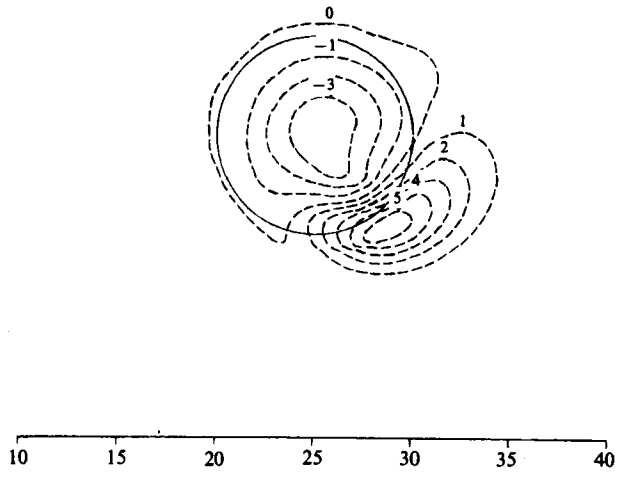

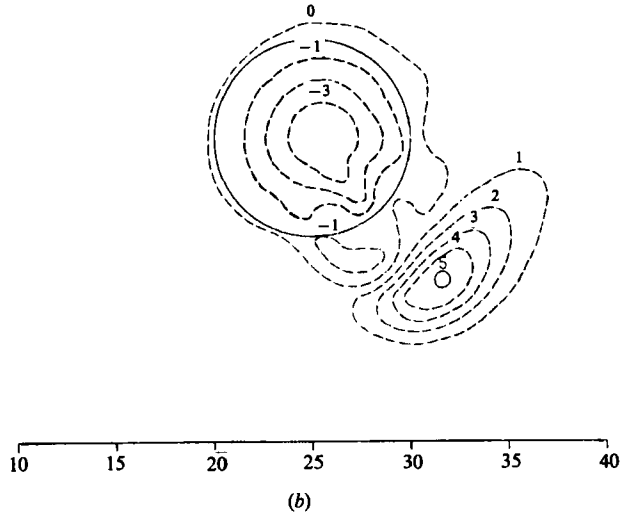

FIGURE 9(*a*,*b*). For caption see facing page.

contours of the non-dimensional vorticity $10\zeta/f$ after 2, 4 and 10 days, shown in figures 8(*b*–*d*). The large positive values to the right of the obstacle corresponds to the trapped vortex, which shows no tendency to drift off downstream even after 10 days.

The total vorticity contained in a bound vortex such as that of figure 8(*d*) can be roughly predicted if it is assumed that the upper surface is horizontal and rigid, and that all the fluid in the vortex comes from upstream. Then conservation of potential

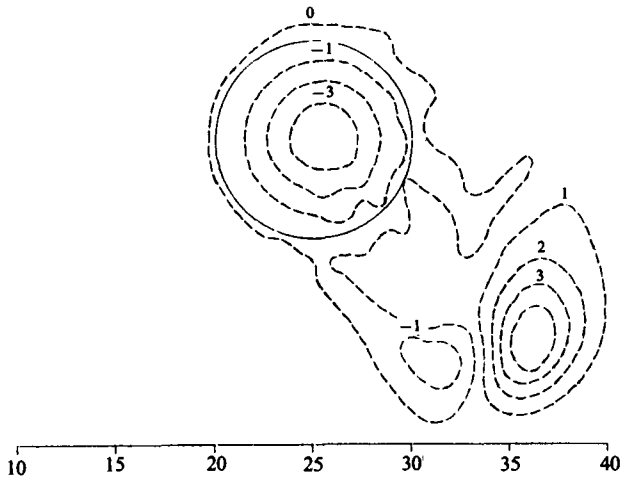

(*c*)

FIGURE 9. Results from the time integration for flow around a cone with $Ro = 0.075$: (*a*), (*b*), (*c*) contours of $10\zeta/f$ after respectively 2, 4, 6 days.

vorticity (3) gives that for the cone given by $h_s/h_0 = h^*(1-a/r)$ the total non-dimensional vorticity over the obstacle is given by

$$\int\int \frac{\zeta}{f}\,\mathrm{d}A = -\int\int \frac{h_s}{h_0}\,\mathrm{d}A = -\frac{\pi}{3}a^2h^*. \tag{28}$$

A similar calculation for the trapped vortex yields a value of $+\frac{1}{3}\pi a^2h^*$. With $h^* = 0.5$ and $a = 5$ km, (28) gives a total vorticity of -13.1 km^2. For the case shown in figure 8(*d*), with the same parameter values, a summation of ζ/f over the gridpoints within the obstacle base gives a value of -12.4 km^2. For the case of figure 8(*d*) a summation of the positive ζ/f over the extent of the trapped vortex gives a comparable value of $+12.5$ km^2. Within the range of the truncation error of the numerical scheme, this value supports the hypothesis that all vorticity is contained in the bound and trapped vortices.

The significance of the trapped-vortex regime depends on its applicability to a real fluid. With even a small amount of viscosity present, the paired-vortex regime may not constitute a steady state. To test this with the present model, the effect of a small vertical velocity induced at the bottom by Ekman pumping is added to the continuity equation (26*b*):

$$\frac{\partial h}{\partial t} + \nabla_{\mathrm{H}}\cdot h\boldsymbol{v}_{\mathrm{H}} - \zeta\left(\frac{K}{2f}\right)^{\frac{1}{2}} = 0, \tag{29}$$

where K is the constant eddy viscosity. The potential-vorticity equation derived from (26*a*, *b*) then has the form

$$\frac{\mathrm{d}}{\mathrm{d}t}\left(\frac{\zeta+f}{h}\right) + \frac{\zeta+f}{h^2}\left(\frac{K}{2f}\right)^{\frac{1}{2}}\zeta = 0. \tag{30}$$

If $f \gg \zeta$ the timescale for spindown is thus $h_0/(K/2f)^{\frac{1}{2}}f$. It was desired to make the ratio of this timescale to the advective scale as large as possible without requiring a prohibitively long integration of the model to determine the resulting final state. A ratio of 10 was chosen (a spindown time of 23 days) and the integration for

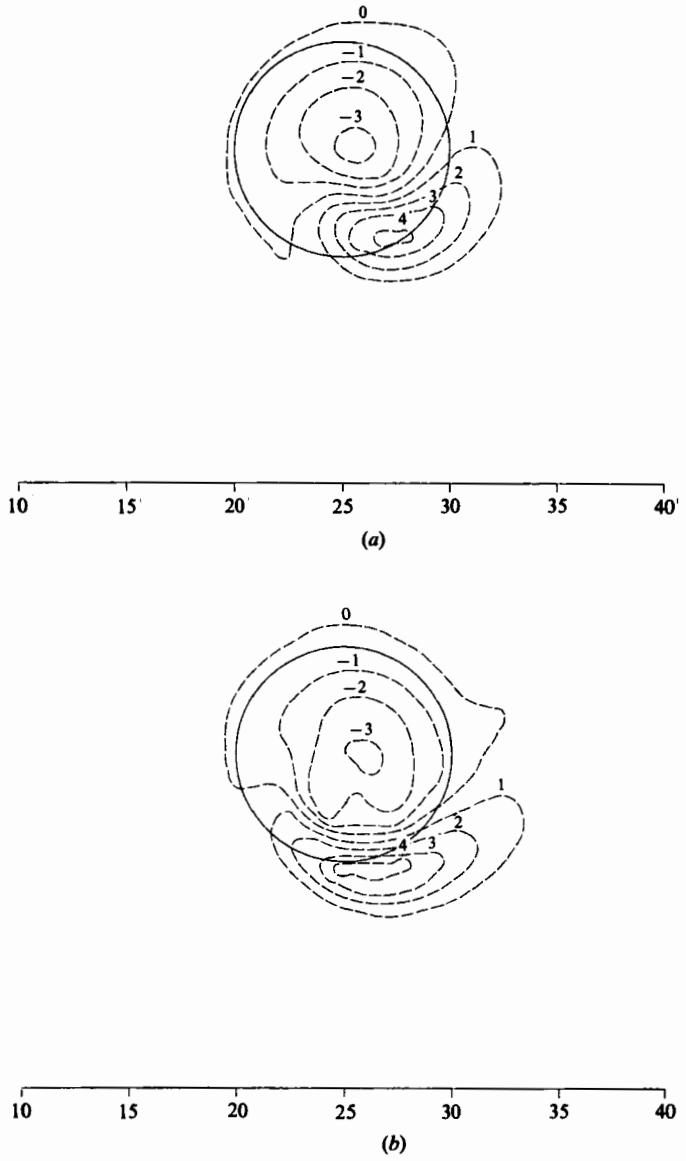

FIGURE 10(*a*, *b*). For caption see facing page.

$Ro = 0.05$ repeated. The non-dimensional vorticity $10\zeta/f$ of the resulting flow after 2 days, shown in figure 10(*a*), is very close to that of figure 8(*b*) – the same case, but without viscosity. However, after 4 days integration (figure 10*b*) the shed eddy is beginning to move, and after 10 days (figure 10*c*) it is clear that the initially trapped vortex is moving off downstream. The result suggests that, in the presence of even a small viscosity, the trapped regime ceases to exist. On consideration, this is not surprising, for in the steady state it can be shown that closed streamlines embedded in regions of positive or negative vorticity cannot exist. If such a situation is postulated, integration of (30) around a streamline indicates that a change of potential vorticity should occur in one circuit, which is contrary to the steady-state

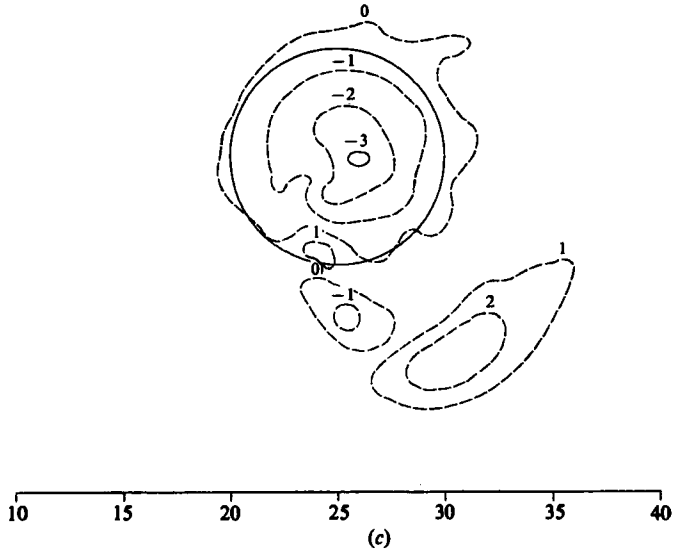

FIGURE 10. Results from the time integration for flow around a cone with $Ro = 0.05$, with small viscosity present: (*a*), (*b*), (*c*) $10\zeta/f$ after respectively 2, 4, 10 days.

assumption. For example, if $\zeta(\zeta+f)$ is of one sign everywhere along the streamline, then the change in potential vorticity in one circuit is given by

$$\Delta\left(\frac{\zeta+f}{h}\right) = -\int_0^L \frac{\mathrm{d}s}{q(s)} \frac{\zeta(\zeta+f)}{h^2} \left(\frac{K}{2f}\right)^{\frac{1}{2}},$$

where L is the length of the streamline and q the speed.

4. Conclusions

Shallow-fluid flow in a channel, with rotation, over and around a single obstacle of simple shape was investigated by means of solution of the steady vorticity equation for quasigeostrophic and finite-Ro flows and by time integration of a numerical model.

Numerical experiments examined, for the regime with no closed streamlines, the dependence of flow deflection on the obstacle dimensions. A measure was proposed to assess quantitatively the flow deflected around the obstacle, and a set of experiments was conducted to determine the dependence of the measure on obstacle volume and aspect ratio. The resulting graphs make possible, within the limitations of the model, prediction of flow pattern from a knowledge of basic flow and obstacle parameters. Deflections increase with volume for fixed aspect ratio and decrease with increasing aspect ratio for fixed volume.

In the regime where closed eddies may exist, time integration of the shallow-water equations was used to test an analytically based hypothesis for the dependence of the flow regime for an axisymmetric obstacle on Rossby number and obstacle height. The existence of a small-Rossby-number regime in which the vorticity originally over the obstacle remains trapped in the vicinity of the obstacle was verified. The elimination of this trapped vortex when a small Ekman suction was introduced was also shown. At a slightly higher Rossby number, in the absence of Ekman suction, a stagnation point is formed and a bound vortex is present over the obstacle, but

no positive vorticity is trapped in the vicinity of the obstacle. At a still larger Rossby number, for which no stagnation points are predicted analytically, the vorticity originally over the obstacle is shed downstream and no closed streamlines exist.

The first author acknowledges the support of the Environmental Protection Agency under Grant CR-807854 and the advice and interest of S. P. S. Arya, principal investigator of that grant. The second author acknowledges the support of the National Science Foundation under Grant ATM 78-16408.

Appendix. The effect of finite boundaries

In the quasigeostrophic theory it is a simple matter to calculate a value for the deflection measure for a conical obstacle of radius a in an unbounded domain for given h^*/Ro. Letting $\psi_g = -u_0 y + \psi'_g$, (4) becomes

$$\frac{1}{r}\frac{\mathrm{d}}{\mathrm{d}r}\left(r\frac{\mathrm{d}\psi'_g}{\mathrm{d}r}\right) = -fh^*\left(1-\frac{r}{a}\right).$$

Hence for $r \leqslant a$

$$\psi_g = -fh^*\left(\frac{r^2}{4}-\frac{r^3}{ya}-\tfrac{5}{36}a^2\right)-u_0 y;$$

for $r \geqslant a$

$$\psi_g = \frac{-fha^2}{6}\ln\frac{r}{a}-u_0 y;$$

and at $x = y = 0$

$$\psi_g = \tfrac{5}{36}fh^* a^2.$$

The deflection m is determined by requiring that ψ_g at $x = -2a$, $y = -am$ is equal to ψ_g at the origin. Hence

$$\tfrac{5}{36}fh^* a^2 = u_0 am - \tfrac{1}{6}fh^* a^2 \ln(4+m^2)^{\frac{1}{2}},$$

or

$$m - \frac{h^*}{6Ro}\ln(4+m^2)^{\frac{1}{2}} = \frac{5}{36}\frac{h^*}{Ro}.$$

At the critical value of h^* ($= \frac{16}{3}Ro$), we find using an iterative procedure that, for $h^*/Ro = \frac{16}{3}$, $m \approx 1.57$.

The quasigeostrophic model was used for the following experiments; the conclusions were then utilized in choosing dimensions in the finite-Ro model, as well as in the finite-difference model.

For the cone ($A = 1$) and the case $h^*/Ro = \frac{16}{3}$, the ratio of channel half-length L_x to obstacle radius l_y was fixed at 5, and the ratio of channel half-width L_y to l_y varied from 3 to 6.5 in steps of 0.50. The values of m for each case are plotted in figure 11, with the dashed line corresponding to a grid resolution of 5 points/l_x, and the solid line to the finer resolution of 10 points/l_x. For this range of values, the decrease in m with the increase of resolution, which gives an estimate of truncation error, is less than 2%. The error incurred due to the presence of sidewalls rather than an infinite plane, estimated from the effect of increasing the channel width, is small, e.g. an increase of L_y/l_x from 5.0 to 6.0 results in an increase in m of only 0.5%. The value $L_y/l_x = 6.0$ was used in the steady experiments of §2.

For larger aspect ratios an analytic value for the deflection is not simple to compute. Thus experiments were conducted, again with $L_x/l_y = 5$, increasing channel width until the curve of m-values appeared to be approaching an asymptote, as shown in figure 2. For $A = 2$, $h^*/Ro = 2.5$ the change in m as shown by the solid line becomes

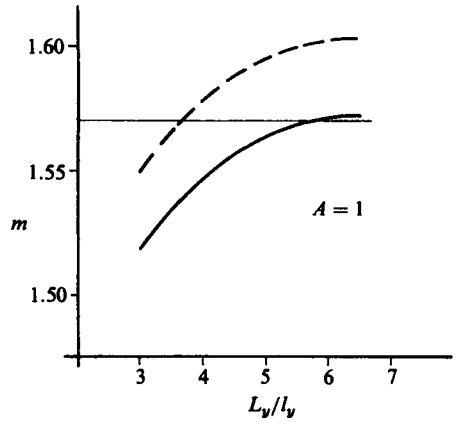

FIGURE 11. Variation of m with channel cross-stream width for a cone ($A = 1$) with a resolution of 5 points/l_x (dashed) and 10 points/l_x (solid); analytically derived value shown as thin solid line.

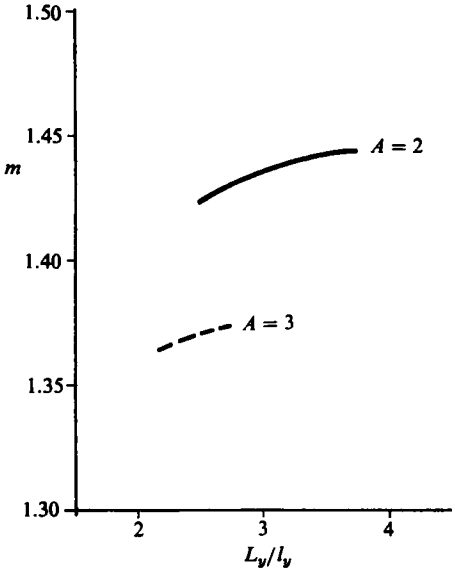

FIGURE 12. Variation of m with width of channel cross-section for $A = 2$ (solid), $A = 3$ (dashed).

acceptably small for $L_y/l_y = 3.5$. For $A = 3$, $h^*/Ro = 2.0$ the change as given by the dashed line was judged to be negligible for $L_y/l_y = 2.5$.

All experiments, both quasigeostrophic and finite-Ro, were carried out with the finer resolution $l_x = 10\Delta s$. For the case $A = 1$ a grid of $100 \times 120\Delta s$ (total length $\times$ total width) was used. For $A = 2$ a channel $100 \times 140\Delta s$ was used; for $A = 3$ the channel measured $100 \times 160\Delta s$.

The finite-difference model used in the time-integration experiments of §3 used the coarser resolution $l_x = 5\Delta s$ (dashed curve in figure 11) and the ratios $L_x/l_y = 5$, $L_y/l_y = 5$. These values were judged to be in an acceptable range for the purposes of that model.

REFERENCES

ARAKAWA, A. & LAMB, V. R. 1983 A potential enstrophy and energy conserving scheme for the shallow water equations. *Mon. Weather Rev.* **109**, 18–36.

BANNON, P. R. 1980 Rotating barotropic flow over finite isolated topography. *J. Fluid Mech.* **101**, 281–306.

HIDE, R. & IBBETSON, A. 1968 On slow transverse flow past obstacles in a rapidly rotating fluid. *J. Fluid Mech.* **32**, 251–272.

HUPPERT, H. E. 1975 Some remarks on the initiation of inertial Taylor columns. *J. Fluid Mech.* **67**, 397–412.

HUPPERT, H. E. & BRYAN, K. 1976 Topographically generated eddies. *Deep-Sea Res.* **23**, 655–679.

INGERSOLL, A. P. 1969 Inertial Taylor columns and Jupiter's Great Red Spot. *J. Atmos. Sci.* **26**, 744–752.

JOHNSON, E. R. 1978 Trapped vortices in rotating flow. *J. Fluid Mech.* **86**, 209–224.

TAYLOR, G. I. 1923 Experiments on the motion of solid bodies in rotating fluids. *Proc. R. Soc. Lond.* A **93**, 99–113.

VAZIRI, A. & BOYER, D. L. 1971 Rotating flow over shallow topographies. *J. Fluid Mech.* **50**, 79–95.